

## APPLICATION OF QUASI-GAS DYNAMIC EQUATIONS TO NUMERICAL SIMULATION OF NEAR-WALL TURBULENT FLOWS

I. A. Shirokov<sup>1</sup> and T. G. Elizarova<sup>2</sup>

UDC 519.63

We describe the possibilities of a numerical method based on quasi-gas dynamic (QGD) equations for the numerical simulation of a turbulent boundary layer. A subsonic Couette flow in nitrogen is used as an example, with dynamic Reynolds numbers of 153 and 198. The QGD system differs from the system of Navier–Stokes equations by additional nonlinear dissipative terms with a small parameter as a coefficient. In turbulent flow simulation, these terms describe small-scale effects that are not resolved on the grid. Comparison of our results (velocity profiles and mean-square velocity pulsations) with direct numerical simulation (DNS) results and benchmark experiments show that the QGD algorithm adequately describes the viscous and the logarithmic layers near the wall. Compared with high-accuracy DNS methods, the QGD algorithm permits using a relatively large spatial grid increment in the interior part of the viscous sublayer. Thus, the total number of grid points in the turbulent boundary layer may be relatively small. Unlike various versions of the large-eddy simulation (LES) method, the QGD algorithm does not require introduction of near-wall functions, because the additional terms vanish near the wall. For small Reynolds numbers, the QGD algorithm describes laminar Couette flow.

**Keywords:** turbulent boundary layer, quasi-gas dynamic equations, subsonic Couette flow, subgrid dissipation.

### Introduction

This article describes for the first time the possibilities of a finite-difference algorithms based on quasi-gas dynamic (QGD) equations for the numerical simulation of a turbulent boundary layer. The gas-dynamic Couette flow in a plane channel is used as an example.

Turbulent gas-dynamic flows near a solid wall in the regions of both viscous and logarithmic sublayer can be described by direct numerical simulation (DNS) using Navier–Stokes equations in compressible or incompressible form [1–3]. However, DNS method require fairly high spatial resolutions, so as to ensure that several grid points are contained in the viscous sublayer. As the Reynold number ( $Re$ ) increases, the computational costs of direct numerical simulation of near-wall flows increase, according to various estimates, in proportion to  $Re^{2.4}$ – $Re^3$  [3, 4]. This is unacceptable for numerical simulation of high-velocity flows even with modern multiprocessor computer systems.

The number of grid points in the near-wall region may be reduced by applying large-eddy simulation (LES) [2, 3]. However, in the immediate vicinity of the wall, subgrid dissipation usually employed in LES model shows nonphysical behavior. So-called near-wall functions [3, 5] have to be introduced to ensure that the wall law holds.

The use of near-wall functions makes it possible to place the first grid point inside the logarithmic sublayer. This reduces the resolution requirements in the boundary layer and the computational costs grow in proportion

---

<sup>1</sup> Faculty of Computational Mathematics and Cybernetics, Moscow State University, Moscow, Russia; e-mail: ivanshirokov@inbox.ru.

<sup>2</sup> Keldysh Institute of Applied Mathematics, Russian Academy of Sciences, Moscow, Russia; e-mail: telizar@mail.ru.

to  $Re^{0.5}$  [3]. However, near-wall function models are without physical substantiation and they should be carefully calibrated for the particular numerical algorithm used and the particular flow investigated. Nevertheless, the near-wall function method has been successfully applied for numerical simulation of non-separating flows and has been extended for simulation of separating flows [3].

In this context, the development of new computational algorithms (less resource-demanding than DNS or without the near-functions required in LES) is an important task for the simulation of both non-separating and separating near-wall turbulent flows.

Because of its simple formulation and the large number of published experimental and numerical simulation results, the Couette flow is often a benchmark for the investigation of numerical algorithms intended for the simulation of non-separating near-wall flows. Reference data are provided by experimental velocity profiles and velocity pulsations in viscous and logarithmic sublayer. Thus, the averaged velocity profiles in turbulent Couette flow, the dependence of the friction coefficient on the Reynolds number, and the empirical formula for this dependence are given in [6, 7]. The profiles of mean-square velocity pulsations near the wall are shown in [8–11]. Detailed studies of the averaged near-wall velocity profile [10, 12, 13] have led to the determination of the numerical coefficients in a two-layer model of near-wall turbulence.

Direct numerical simulation (DNS) of turbulent Couette flow has been carried out in [4, 11, 14–16]. The results of [11] fit the experimental data from [6–10]. The results of [4, 14–16] also reasonably agree with experimental data. However, the constants of the two-layer turbulence model obtained in [4, 14–16] are somewhat smaller than the experimental values from [6–10].

As an alternative approach to numerical simulation of turbulent flows of viscous compressible gas, the authors propose the so-called system of quasi-gas dynamic (QGD) equations and a numerical algorithm based on this system (QGD algorithm).

The QGD equations are based on smoothed (regularized) Navier–Stokes equations [17–19]. These equations were proposed more than 30 years ago for modeling supersonic ideal-gas flows. The QGD system differs from the Navier–Stokes system by the presence of dissipative terms, whose value is determined by the parameter  $\tau$  ( $\tau$ -terms). These terms act as adaptive regularizers that stabilize the numerical solutions in zones with large parameter gradients, but become vanishingly small in regions of stationary smooth flow. In the asymptotic boundary layer approximation [1], the  $\tau$ -terms vanish and the QGD equations reduce to classical Prandtl equations, similarly to the Navier–Stokes system [18].

One of the advantages of QGD numerical algorithms is that they dispense with separated grids and various monotization procedures. All spatial variables can be approximated by central differences in a time-explicit finite-difference scheme. Many examples of successful applications of the QGD algorithm to a wide range of nonstationary subsonic and supersonic gas-dynamic flows can be found in [17–20], and also in references cited therein and below.

In particular, the QGD system has been used in [20] to construct and apply an algorithm for the simulation of magnetohydrodynamic (MHD) ideal-gas flows. The accuracy and the convergence of the proposed method have been confirmed by numerous standard MHD tests, including the three-dimensional supersonic inviscid Orszag–Tang flow (vortex).

Recent studies [19, 20] review the results obtained using the QGD model, including supersonic and subsonic tests and theoretical conclusions. In the present article, we do not repeat this review.

Extensive computational experience shows that the QGD algorithm is highly promising for the simulation of turbulent flows with moderate Reynolds numbers.

The first systematic study of the possibilities of the QGD algorithm for the simulation of turbulence has been carried out for viscous Taylor–Green flow (vortex) in free space [21]. The calculations have been performed for turbulent and laminar regimes, include laminar-turbulent transition, with Reynolds numbers from 100 to 5000. Nitrogen flow under normal temperatures has been considered. The  $\tau$ -terms regularize the

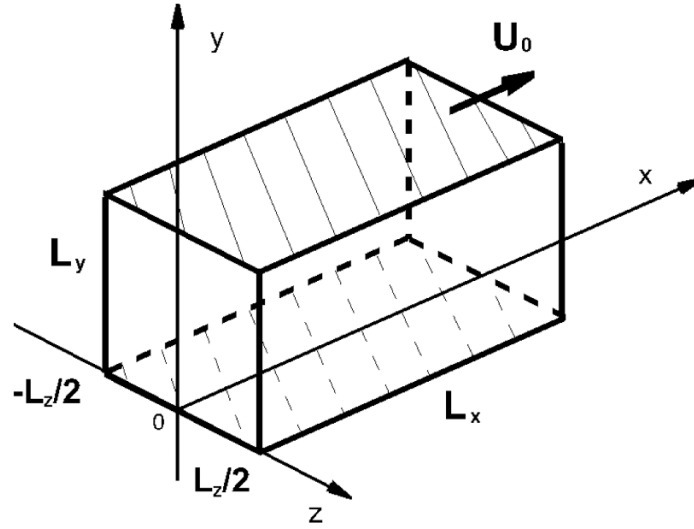


**Fig. 1.** A general scheme of the numerical region.

numerical solution for laminar flows and in the turbulent case they ensure the mechanism of subgrid dissipation averaging the flow singularities that are not resolved on the grid. Investigations show that the QGD algorithm requires fewer grid points to attain the same accuracy as the DNS methods. At the same time, the QGD algorithm is more accurate than LES with the same number of points. A brief history of QGD models and their construction by time-averaging of the Navier–Stokes systems is presented in [21], where we also find a brief description of the corresponding finite-difference algorithms.

Simulation of turbulent flows near surfaces is of considerable interest in applications. In the present article we investigate for the first time the possibilities of the QGD algorithm for the simulation of near-wall turbulent flows. As an example we use canonical plane Couette flow between two infinite planes with nitrogen at normal temperature.

Section 2 describes the statement of the problem and presents the values of the gas-dynamic parameters. Section 3 gives the QGD equations in Cartesian coordinates, which are useful for the implementation of the numerical algorithm. Section 4 provides general remarks concerning the numerical algorithm, including the determination of tuning parameters and averaged variables.

A detailed presentation of the numerical simulation results for  $Re = 3000$  (which corresponds to dynamic Reynolds number  $Re_\tau = 153$ ) is given in Section 5. Section 6 presents the main results for  $Re = 4250$  ( $Re_\tau = 198$ ).

The simulation results for the laminar case ( $Re = 300$ ) and comparison of friction coefficients for various Reynolds numbers are presented in Sections 7 and 8, respectively. In conclusion we provide a brief review of our results and the prospects for the application of the QGD algorithm to turbulent flow simulation.

## 2. Statement of the Problem

Consider a three-dimensional numerical region in Cartesian coordinates  $0 \leq x \leq L_x$ ,  $0 \leq y \leq L_y$ ,  $-L_z/2 \leq z \leq L_z/2$  (see Fig. 1).

The boundary  $y = 0$  is a stationary solid wall. The opposite boundary  $y = L_y$  is a solid wall that moves with constant velocity  $U_0$  in the direction of positive  $x$ . The region is filled with nitrogen. The state of the

gas is described by the density  $\rho(x, y, z, t)$ , the macroscopic velocity components  $u_x(x, y, z, t)$ ,  $u_y(x, y, z, t)$ ,  $u_z(x, y, z, t)$ , and the pressure  $p(x, y, z, t)$ . Ideal gas is assumed:  $p = \rho RT$ . Table 1 lists the values of the gas-dynamic parameters.

**Table 1**  
**Gas-Dynamic Parameters**

$R = 297 \text{ J}/(\text{kg} \cdot \text{K})$	Nitrogen gas constant
$\gamma = 7/5$	Nitrogen adiabatic index
$Pr = 14/19$	Nitrogen Prandtl number
$T_0 = 273 \text{ K}$	Initial temperature
$\mu = \mu_0(T/T_0)^\omega$	Nitrogen viscosity as a function of temperature
$\mu_0 = 1.67 \cdot 10^{-5} \text{ kg}/(\text{m} \cdot \text{sec})$	Nitrogen viscosity at $T_0 = 273 \text{ K}$
$\omega = 0.74$	Intermolecular interaction index
$U_0 = 168.5 \text{ m}/\text{sec}$	Velocity of channel wall
$c_S = \sqrt{\gamma RT}$	Velocity of sound
$c_{S0} = \sqrt{\gamma RT_0} = 337 \text{ m}/\text{sec}$	Velocity of sound at initial conditions
$Ma = U_0/c_{S0} = 0.5$	Initial Mach number

The initial temperature is constant in the entire region:  $T = T_0 = 273 \text{ K}$ . Initial pressure and density are also constant and are determined by the equation of state.

The boundary conditions are periodic along the axes  $x$  and  $z$ . On the solid walls we impose sticking conditions ( $u_x = u_y = u_z = 0$  for  $y = 0$ ;  $u_x = U_0$ ,  $u_y = u_z = 0$  for  $y = L_y$ ), and also the conditions  $\partial T/\partial n = 0$ ,  $\partial p/\partial n = 0$  and  $\partial \rho/\partial n = 0$ , because the walls are assumed adiabatic.

As the initial condition for the longitudinal velocity we use the incompressible-flow laminar profile

$$u_x = U_0 y/L_y. \quad (1)$$

For small initial Reynolds numbers  $Re = \rho_0(U_0/2)(L_y/2)/\mu_0$  the flow is laminar. As  $Re$  increases, transition to turbulent flow is observed.

The onset of turbulent flow (the choice of the initial disturbance whose evolution leads in the fastest way to the establishment of a non-steady state oscillatory process) is a complex mathematical problem. As a rule, for this disturbance we choose the least stable eigenfunctions of the boundary-value problem for the Orr–Sommerfeld equation (Tollmien–Schlichting waves) [3, 11, 22].

In this study, we introduce a simple initial disturbance in the transverse velocity components:

$$u_y = u_z = 0.2U_0 \sin(8\pi x/L_x). \quad (2)$$

Furthermore, additional small velocity disturbances (turbulizers) are introduced along the edges of the numerical region. Specifically, the velocity components on the four edges parallel to the flow velocity are not equal to the wall velocity: they are taken from the neighboring grid cell.

### 3. Mathematical Model

We describe turbulent gas flow by a macroscopic system of QGD equations [17–19], a brief derivation of which is given in [21]. The QGD system defines the evolution in time of gas density, velocity, and pressure that depend on Eulerian coordinates and on time. The QGD system in Cartesian coordinates has the form

$$\frac{\partial}{\partial t} \rho + \nabla_i j_m^i = 0, \quad (3)$$

$$\frac{\partial}{\partial t} \rho u^j + \nabla_i (j_m^i u^j) + \nabla^j p = \nabla_i \Pi^{ij}, \quad (4)$$

$$\frac{\partial}{\partial t} E + \nabla_i (j_m^i H) + \nabla_i q^i = \nabla_i (\Pi^{ij} u_j). \quad (5)$$

The total energy per unit volume  $E$  and the total specific enthalpy  $H$  are calculated from the formulas  $E = \rho u^2/2 + p/(\gamma - 1)$  and  $H = (E + p)/\rho$ . The mass flux density vector  $j_m^i$  is defined as

$$j_m^i = \rho(u^i - w^i), \quad w^i = \frac{\tau}{\rho} (\nabla_j \rho u^i u^j + \nabla^i p). \quad (6)$$

The expressions for the viscous stress tensor  $\Pi^{ij}$  and the heat flux  $q^i$  are written as

$$\Pi^{ij} = \Pi_{NS}^{ij} + \tau u_i \rho \left( u_k \nabla^k u_j + \frac{1}{\rho} \nabla_j p \right) + \tau \delta^{ij} (u_k \nabla^k p + \gamma p \nabla^k u_k), \quad (7)$$

$$\Pi_{NS}^{ij} = \mu (\nabla^i u^j + \nabla^j u^i - \frac{2}{3} \nabla^k u_k) + \zeta \delta^{ij} \nabla^k u_k, \quad (8)$$

$$q^i = q_{NS}^i - \tau u_i \rho \left( u_j \nabla^j \varepsilon + p u_j \nabla^j \frac{1}{\rho} \right), \quad q_{NS}^i = -\kappa \nabla^i T. \quad (9)$$

Here  $\delta$  is the Kronecker delta ( $\delta^{ij} = 1$  for  $i = j$  and  $\delta^{ij} = 0$  for  $i \neq j$ ) and  $\varepsilon = p/(\rho(\gamma - 1))$  is the internal energy per unit gas mass.  $\Pi_{NS}^{ij}$  and  $q_{NS}^i$  are the viscous stress tensor and the heat flux in the Navier–Stokes system.

The thermal conductivity is expressed by the relationship [19]

$$\kappa = \frac{\mu\gamma R}{\text{Pr}(\gamma - 1)}, \quad (10)$$

where  $\text{Pr}$  is the Prandtl number [19, 23]. The dynamic viscosity  $\mu$  in expressions (7)–(10) for  $\Pi_{NS}^{\dot{ij}}$  and  $q_{NS}^i$  is defined by the temperature dependence [19]

$$\mu = \mu_0(T/T_0)^\omega, \quad (11)$$

where  $\omega$  describes the intermolecular interaction in the gas [23]. The second (volume) viscosity is defined by the relationship [19]

$$\zeta = \mu(5/3 - \gamma). \quad (12)$$

The relaxation parameter  $\tau$  in (6)–(9) is defined as

$$\tau = \alpha h/c_s, \quad (13)$$

where  $c_s = \sqrt{\gamma RT}$  is the local velocity of sound and  $h$  is the spatial grid increment. The terms with the coefficient  $\tau$  represent subgrid dissipation, which smooths out the pulsations of the gas-dynamic variables on scales of the order of the grid increment. The coefficient  $\alpha$  may be treated as the tuning parameter that determines the magnitude of subgrid dissipation.

We rewrite system (3)–(9) in the variables  $x$ ,  $y$ ,  $z$  in a form convenient for the construction of the numerical algorithm.

The equation for density:

$$\frac{\partial}{\partial t} \rho + \frac{\partial}{\partial x} j_{mx} + \frac{\partial}{\partial y} j_{my} + \frac{\partial}{\partial z} j_{mz} = 0, \quad (14)$$

where

$$j_{mx} = \rho u_x - \tau \frac{\partial}{\partial x} (\rho u_x^2 + p) - \tau \frac{\partial}{\partial y} \rho u_x u_y - \tau \frac{\partial}{\partial z} \rho u_x u_z, \quad (15)$$

$$j_{my} = \rho u_y - \tau \frac{\partial}{\partial x} \rho u_x u_y - \tau \frac{\partial}{\partial y} (\rho u_y^2 + p) - \tau \frac{\partial}{\partial z} \rho u_y u_z, \quad (16)$$

$$j_{mz} = \rho u_z - \tau \frac{\partial}{\partial x} \rho u_x u_z - \tau \frac{\partial}{\partial y} \rho u_y u_z - \tau \frac{\partial}{\partial z} (\rho u_z^2 + p). \quad (17)$$

The equation for the momentum  $x$ -component:

$$\frac{\partial}{\partial t} \rho u_x = \frac{\partial}{\partial x} (\Pi_{xx} - j_{mx} u_x - p) + \frac{\partial}{\partial y} (\Pi_{yx} - j_{my} u_x) + \frac{\partial}{\partial z} (\Pi_{zx} - j_{mz} u_x), \quad (18)$$

where

$$\begin{aligned} \Pi_{xx} = & \left( \left[ \frac{4}{3} \mu + \zeta \right] + \tau \gamma p + \tau \rho u_x^2 \right) \frac{\partial}{\partial x} u_x + 2\tau u_x \frac{\partial}{\partial x} p + \left( -\frac{2}{3} \mu + \zeta + \tau \gamma p \right) \frac{\partial}{\partial y} u_y \\ & + \tau u_y \frac{\partial}{\partial y} p + \tau \rho u_x u_y \frac{\partial}{\partial y} u_x + \left( -\frac{2}{3} \mu + \zeta + \tau \gamma p \right) \frac{\partial}{\partial z} u_z + \tau u_z \frac{\partial}{\partial z} p + \tau \rho u_x u_z \frac{\partial}{\partial z} u_x, \end{aligned} \quad (19)$$

$$\Pi_{yx} = \left( \mu + \tau \rho u_y^2 \right) \frac{\partial}{\partial y} u_x + \mu \frac{\partial}{\partial x} u_y + \tau \rho u_y u_x \frac{\partial}{\partial x} u_x + \tau \rho u_y u_z \frac{\partial}{\partial z} u_x + \tau u_y \frac{\partial}{\partial x} p, \quad (20)$$

$$\Pi_{zx} = \left( \mu + \tau \rho u_z^2 \right) \frac{\partial}{\partial z} u_x + \mu \frac{\partial}{\partial x} u_z + \tau \rho u_z u_x \frac{\partial}{\partial x} u_x + \tau \rho u_z u_y \frac{\partial}{\partial y} u_x + \tau u_z \frac{\partial}{\partial x} p. \quad (21)$$

The equation for the momentum  $y$ -component:

$$\frac{\partial}{\partial t} \rho u_y = \frac{\partial}{\partial x} (\Pi_{xy} - j_{mx} u_y) + \frac{\partial}{\partial y} (\Pi_{yy} - j_{my} u_y - p) + \frac{\partial}{\partial z} (\Pi_{zy} - j_{mz} u_y), \quad (22)$$

where

$$\Pi_{xy} = \left( \mu + \tau \rho u_x^2 \right) \frac{\partial u_y}{\partial x} + \mu \frac{\partial u_x}{\partial y} + \tau \rho u_x u_y \frac{\partial u_y}{\partial y} + \tau \rho u_x u_z \frac{\partial u_y}{\partial z} + \tau u_x \frac{\partial p}{\partial y}, \quad (23)$$

$$\begin{aligned} \Pi_{yy} = & \left( \frac{4}{3} \mu + \zeta + \tau \gamma p + \tau \rho u_y^2 \right) \frac{\partial u_y}{\partial y} + 2\tau u_y \frac{\partial p}{\partial y} + \left( -\frac{2}{3} \mu + \zeta + \tau \gamma p \right) \frac{\partial u_x}{\partial x} \\ & + \tau \rho u_y u_x \frac{\partial u_y}{\partial x} + \tau u_x \frac{\partial p}{\partial x} + \left( -\frac{2}{3} \mu + \zeta + \tau \gamma p \right) \frac{\partial u_z}{\partial z} + \tau \rho u_y u_z \frac{\partial u_y}{\partial z} + \tau u_z \frac{\partial p}{\partial z}, \end{aligned} \quad (24)$$

$$\Pi_{zy} = \left( \mu + \tau \rho u_z^2 \right) \frac{\partial u_y}{\partial z} + \mu \frac{\partial u_z}{\partial y} + \tau \rho u_z u_x \frac{\partial u_y}{\partial x} + \tau \rho u_z u_y \frac{\partial u_y}{\partial y} + \tau u_z \frac{\partial p}{\partial y}. \quad (25)$$

The equation for the momentum  $z$ -component:

$$\frac{\partial}{\partial t} \rho u_z = \frac{\partial}{\partial x} (\Pi_{xz} - j_{mx} u_z) + \frac{\partial}{\partial y} (\Pi_{yz} - j_{my} u_z) + \frac{\partial}{\partial z} (\Pi_{zz} - j_{mz} u_z - p), \quad (26)$$

where

$$\Pi_{xz} = \left( \mu + \tau \rho u_x^2 \right) \frac{\partial u_z}{\partial x} + \mu \frac{\partial u_x}{\partial z} + \tau \rho u_x u_y \frac{\partial u_z}{\partial y} + \tau \rho u_x u_z \frac{\partial u_z}{\partial z} + \tau u_x \frac{\partial p}{\partial z}, \quad (27)$$

$$\Pi_{yz} = \left( \mu + \tau \rho u_y^2 \right) \frac{\partial u_z}{\partial y} + \mu \frac{\partial u_y}{\partial z} + \tau \rho u_y u_x \frac{\partial u_z}{\partial x} + \tau \rho u_y u_z \frac{\partial u_z}{\partial z} + \tau u_y \frac{\partial p}{\partial z}, \quad (28)$$

$$\begin{aligned} \Pi_{zz} = & \left( \frac{4}{3} \mu + \zeta + \tau \gamma p + \tau \rho u_z^2 \right) \frac{\partial u_z}{\partial z} + 2 \tau u_z \frac{\partial p}{\partial z} + \left( -\frac{2}{3} \mu + \zeta + \tau \gamma p \right) \frac{\partial u_x}{\partial x} \\ & + \tau \rho u_z u_x \frac{\partial u_z}{\partial x} + \tau u_x \frac{\partial p}{\partial x} + \left( -\frac{2}{3} \mu + \zeta + \tau \gamma p \right) \frac{\partial u_y}{\partial y} + \tau \rho u_z u_y \frac{\partial u_z}{\partial y} + \tau u_y \frac{\partial p}{\partial y}. \end{aligned} \quad (29)$$

The equation for total energy:

$$\begin{aligned} \frac{\partial}{\partial t} E = & \frac{\partial}{\partial x} \left( \Pi_{xx} u_x + \Pi_{xy} u_y + \Pi_{xz} u_z - j_{mx} H - q_x \right) \\ & + \frac{\partial}{\partial y} \left( \Pi_{yx} u_x + \Pi_{yy} u_y + \Pi_{yz} u_z - j_{my} H - q_y \right) \\ & + \frac{\partial}{\partial z} \left( \Pi_{zx} u_x + \Pi_{zy} u_y + \Pi_{zz} u_z - j_{mz} H - q_z \right), \end{aligned} \quad (30)$$

where

$$H = \frac{1}{2} \left( u_x^2 + u_y^2 + u_z^2 \right) + \frac{\gamma}{\gamma - 1} \frac{p}{\rho}, \quad (31)$$

$$q_x = -\kappa \frac{\partial T}{\partial x} - u_x R_q, \quad q_y = -\kappa \frac{\partial T}{\partial y} - u_y R_q, \quad q_z = -\kappa \frac{\partial T}{\partial z} - u_z R_q, \quad (32)$$

$$\begin{aligned} R_q = & \tau \rho \frac{1}{\gamma - 1} \left\{ u_x \frac{\partial}{\partial x} \left( \frac{p}{\rho} \right) + u_y \frac{\partial}{\partial y} \left( \frac{p}{\rho} \right) + u_z \frac{\partial}{\partial z} \left( \frac{p}{\rho} \right) \right\} \\ & + \tau \rho p \left\{ u_x \frac{\partial}{\partial x} \left( \frac{1}{\rho} \right) + u_y \frac{\partial}{\partial y} \left( \frac{1}{\rho} \right) + u_z \frac{\partial}{\partial z} \left( \frac{1}{\rho} \right) \right\}. \end{aligned} \quad (33)$$

The components  $\Pi^{ij}$  and  $j_m^i$  in (30) are defined by (15)–(29).

The stationary laminar Couette flow is one of the examples for which the exact solution of the Navier–Stokes equations is known for all Mach and Reynolds numbers. This solution for a compressible heat-



conducting gas has been proposed and investigated by Illingworth [24]. Following [18], we show that Illingworth's solution is also the exact solution for the QGD system (14)–(33).

An analytical solution for Couette flow can be constructed assuming that the gas-dynamic parameters depend only on the normal coordinate  $y$ :

$$u_x = u_x(y), \quad u_y = 0, \quad u_z = 0, \quad p = p(y), \quad \rho = \rho(y).$$

Taking  $p = \rho RT$ , we obtain  $T = T(y)$ . Substituting these expressions in Eqs. (14)–(33), we obtain the components in a simplified form:

$$j_{mx} = \rho u_x, \quad j_{my} = -\tau \frac{dp}{dy}, \quad j_{mz} = 0,$$

$$\Pi_{xx} = \Pi_{yy} = \Pi_{zz} = 0, \quad \Pi_{xz} = \Pi_{zx} = \Pi_{yz} = \Pi_{zy} = 0,$$

$$\Pi_{yx} = \mu \frac{du_x}{dy}, \quad \Pi_{xy} = \mu \frac{du_x}{dy} + \tau u_x \frac{dp}{dy},$$

$$R_q = 0, \quad q_x = q_z = 0, \quad q_y = -\kappa \frac{dT}{dy}.$$

Equations (14), (18), (22), (26), and (33) thus reduce to the form

$$\frac{d}{dy} \left( \tau \frac{dp}{dy} \right) = 0, \quad \frac{d}{dy} \left( \mu \frac{du_x}{dy} \right) + \frac{d}{dy} \left( \tau u_x \frac{dp}{dy} \right) = 0,$$

$$\frac{d}{dy} \left( \mu u_x \frac{du_x}{dy} \right) + \frac{d}{dy} \left( \kappa \frac{dT}{dy} \right) + \frac{d}{dy} \left( \tau H \frac{dp}{dy} \right) = 0,$$

$$\frac{dp}{dy} = 0.$$

Noting the last equation, we conclude that the flow pressure is constant. Hence it follows that all the  $\tau$ -terms vanish. The system thus takes the form

$$\frac{d}{dy} \left( \mu \frac{du_x}{dy} \right) = 0,$$

$$\frac{d}{dy} \left( \mu u_x \frac{du_x}{dy} \right) + \frac{d}{dy} \left( \kappa \frac{dT}{dy} \right) = 0.$$

These equations are identical with the system obtained for the stationary Couette flow from Navier–Stokes equations [24]. Thus, the analytical solution of the Navier–Stokes system for Couette flow is also the exact solution of the QGD system. This analytical solution can be obtained in implicit form for a gas of Maxwellian molecules ( $\omega = 1$ ) with boundary conditions of a special form (sticking condition for the velocity, isothermal and adiabatic conditions for top and bottom walls, respectively). For small Mach numbers, the Illingworth solution is almost identical with the expression for incompressible fluid (1).

For Poiseuille flow and many other known problems, we can show that the exact solutions of stationary Navier–Stokes equations are also exact solution of QGD equations [18].

#### 4. Numerical Algorithm: General Remarks

To solve the initial–boundary-value problem (3)–(33) with initial conditions (1) and (2) by finite differences, we introduce a spatially and temporally uniform grid

$$\begin{aligned} \Omega_{xyzt} &= \omega_x \times \omega_y \times \omega_z \times \omega_t, & \omega_x &= \{x_i, i = \overline{0, N_x - 1}, x_i = -h/2 + hi\}, \\ \omega_y &= \{y_j, j = \overline{0, N_y - 1}, y_j = -h/2 + hj\}, & \omega_z &= \{z_k, k = \overline{0, N_z - 1}, z_k = -L_z/2 - h/2 + hk\}, \\ \omega_t &= \{t, n_t = \overline{0, N_t}, t = h_t n_t\}. \end{aligned}$$

The number of time steps  $N_t$  is not given in advance. The region boundaries are at the half-integer points.

The algorithm that constructs the time-explicit scheme is the same as in [21, 25, 26]: the spatial derivatives are approximated to second order by central differences and the explicit Euler method is used for the time derivatives.

The computations have been carried out on the K-100 multiprocessor computer system [27], with parallelization achieved by partitioning the numerical region by the planes  $x = \text{const}$ . This technology uses the MPI message transmission technology and has been successfully applied in [21, 25, 26]. The software system is fully transportable across platforms that support the C language and the MPI standard.

The values of the computational parameters are given in Table 2.

The QGD algorithm used in this study has a single tuning parameter  $\alpha$  that determines the level of subgrid dissipation. The effect of this parameter on numerical solution for laminar flows and flows with shocks has been investigated by the authors in earlier studies. We have shown that relatively large values of  $\alpha$  produce excessive smoothing of the solution, while small values of  $\alpha$  may cause spurious oscillations in regions with large parameter gradients.

For most flows, the suitable values are in the range  $0.05 < \alpha < 0.5$ . The effect of the coefficient  $\alpha$  on the simulation of turbulent flows has been investigated in [21]. With the Taylor–Green vortex it has been shown that  $\alpha = 0.1$  is optimal for the simulation of free turbulent flows far from the walls. The results of the present study suggest the same value  $\alpha = 0.1$  for the simulation of near-wall turbulent flows.

In the present study we simulate the Couette flow for three values of the initial Reynolds number  $Re = 3000, 4250, \text{ and } 300$ . With the exception of the initial values of density and pressure (which are determined by  $Re$ ), all computational parameters are the same for the three cases. The procedure of specifying the initial values of the gas parameters from given Mach and Reynolds numbers is the same as in [21].

**Table 2**  
**Computational Parameters**

$L_x = 0.16$ m	Channel length
$L_y = 0.08$ m	Distance between solid walls (channel height)
$L_z = 0.08$ m	Channel width
$N_x = 162$ , $N_y = 82$ , $N_z = 82$	Size of difference grid
$h = 0.001$ m	Grid increment
$h_t = \beta h / c_{S0} = 5.936 \cdot 10^{-7}$ sec	Time increment
$\beta = 0.2$	Courant number
$\tau = \alpha h / c_s$	Relaxation parameter
$\alpha = 0.1$	Tuning parameter

**Table 3**  
**Dynamic Parameters**

$Re = \rho_0 (U_0/2)(L_y/2) / \mu_0$	Initial Reynolds number
$Re^m = (\rho^m (U_0/2)(L_y/2) / \mu^m)  _{y=0}$	Averaged Reynolds number
$Re_\tau = (\rho^m u_\tau (L_y/2) / \mu^m)  _{y=0}$	Dynamic Reynolds number
$u_x^m$ , $\mu^m$ , $\rho^m$	Time-averaged velocity, dynamic viscosity, and density
$u_\tau = \left( (\tau_w / \rho^m)^{1/2} \right)  _{y=0}$	Dynamic velocity
$l_\tau = \left( \mu^m / (\rho^m u_\tau) \right)  _{y=0}$	Dynamic length
$\tau_w = \left( \mu^m (du_x^m / dy) \right)  _{y=0}$	Tangential stress on the wall
$u_+ = u_x^m / u_\tau$	Dimensionless velocity
$y_+ = y / l_\tau$	Dimensionless coordinate
$C_f = 2\tau_w / \left( \rho^m (U_0/2)^2 \right)$	Friction coefficient

With  $Re = 3000$  and  $Re = 4250$ , the initial disturbance (2) leads to the development of turbulent Couette flow. With  $Re = 300$ , the initial disturbance is rapidly smoothed out due to viscous dissipation and laminar Couette flow is formed.

Table 3 lists the dynamic flow parameters.

Here  $\mu^m$ ,  $\rho^m$  are the time-averaged values of  $\mu$  and  $\rho$  at the point  $x = L_x/2$ ,  $y = 0$ ,  $z = 0$  (in the middle of the bottom wall). The parameter  $u_x^m$  is the time-averaged longitudinal velocity component  $u_x$  in the cross-section  $x = L_x/2$ ,  $z = 0$ . Time-averaging is performed according to the formula (shown for the case of the velocity component  $u_x$ )

$$u_x^m = \frac{1}{n_{t2} - n_{t1} + 1} \left( \sum_{n_i=n_{t1}}^{n_{t2}} u_x \right). \quad (34)$$

The time-step indices  $n_{t1}$  and  $n_{t2}$  are the ends of the averaging interval. Formula (34) may be written as a recurrence, which is convenient for program implementation:

$$u_x^m \Big|_{n_{t2}+1} = \frac{n_{t2} - n_{t1} + 1}{n_{t2} - n_{t1} + 2} u_x^m \Big|_{n_{t2}} + \frac{1}{n_{t2} - n_{t1} + 2} u_x \Big|_{n_{t2}+1}. \quad (35)$$

Here the mean velocity in step  $n_{t2} + 1$  is calculated from the mean velocity in the preceding step  $n_{t2}$ .

For  $Re = 3000$  and  $Re = 4250$  averaging is from  $n_{t1} = 3 \cdot 10^5$  to  $n_{t2} = 8 \cdot 10^5$ . Note that the total number of time steps  $n_{t2} = 8 \cdot 10^5$  corresponds to  $t = 0.475$  sec and takes about 160 hours of machine time on the 32-processor K-100 cluster (Intel Xeon X5670 processors) [27]. The averaging time  $T^m = h_t(n_{t2} - n_{t1}) = 0.297$  sec can be expressed in terms of the channel half-height  $L_y/2$  and the axial flow velocity  $U_0/2$ :  $T^m = 625 \left( (L_y/2)/(U_0/2) \right)$ .

Energy dissipation of the initial disturbance (2) raises the gas temperature above the initial temperature  $T_0$ . In turbulent flow, the temperature is maximal near the walls, whereas in laminar flow the temperature is virtually constant throughout the numerical region. Since the gas viscosity is a function of temperature according to (11), the viscosity in steady-state flow also exceeds the initial value  $\mu_0$ .

**Table 4**  
**Values of Dynamic Parameters in the Present Study**

Flow	Re	Re <sup>m</sup>	Re <sub>τ</sub>	C <sub>f</sub>
Laminar	300	286	17	0.007
Turbulent	3000	2804	153	0.0059
Turbulent	4250	3994	198	0.0049

To allow for this effect, we introduced the averaged Reynolds number  $Re^m$  calculated from the averaged values of  $\mu^m$  and  $\rho^m$ .  $Re^m$  turns out to be somewhat smaller than the initial Re. The values of the dynamic parameters obtained in our calculations are shown in Table 4. Note that the conventional models for viscous incompressible flows ignore heating due to kinetic energy dissipation.

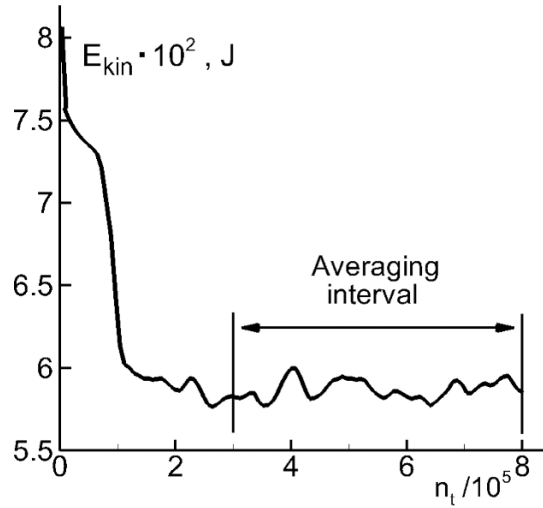


**Fig. 2.** Gas kinetic energy as a function of the current number of time steps for  $Re = 3000$ .

The gas kinetic energy in the numerical region is determined by the formula

$$E_{kin}(t) = \sum_{i=1}^{N_x-2} \sum_{j=1}^{N_y-2} \sum_{k=1}^{N_z-2} \frac{1}{2} \rho_{ijk}(t) \left( u_{xijk}^2(t) + u_{yijk}^2(t) + u_{zijk}^2(t) \right) \cdot h^3, \quad (36)$$

where summation is over the points of the spatial grid.

## 5. Calculation Results for $Re = 3000$

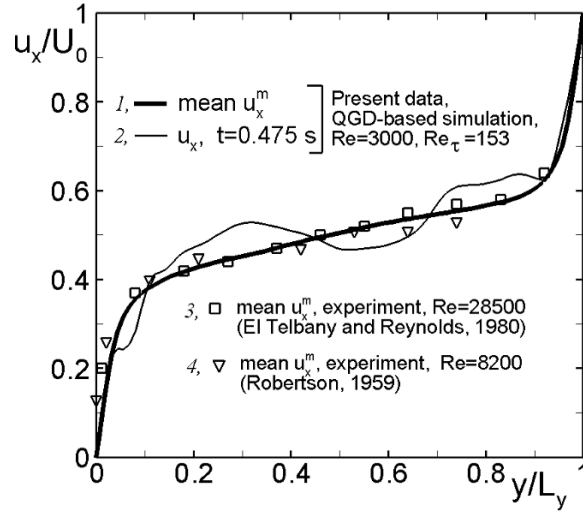
Figure 2 plots the dependence of the gas kinetic energy in the numerical region (36) on the current number of time steps  $n_t$  (here  $t = h_t n_t$ ). After  $n_t = 2 \cdot 10^5$  a turbulent regime is established and the kinetic energy profile become quasi-periodic.

Figure 3 shows the calculated profile of the time-averaged longitudinal velocity component  $u_x^m$  as a function of the coordinate  $y$  (curve 1). The mean velocity  $u_x^m$  is normalized by the wall velocity  $U_0$ , the coordinate  $y$  is normalized by the channel height  $L_y$ .

In Figure 3, markers 3 and 4 show the experimental profiles of the mean longitudinal velocity in Couette flow for  $Re = 28,500$  [7, 11] and  $Re = 8,200$  [6, 11], respectively. The results for different Reynolds numbers are not much different. We see that QGD simulation faithfully reproduces the mean velocity characteristic profile in Couette flow.

Alongside the mean velocity profile  $u_x^m$ , Fig. 3 shows the instantaneous velocity  $u_x$  (curve 2) at time  $t = 0.475$  sec. While the mean velocity profile has the characteristic shape of turbulent flow in a channel, the instantaneous velocity exhibits random oscillations. These oscillations are described below in Figs. 5–7.

Figure 4 shows the calculated profile of the mean velocity  $u_x^m$  in dimensionless coordinates (markers 1) and also the data obtained in experimental studies of Couette flow [10]. The results for  $Re = 9,500$  and  $Re = 18,960$  are designated by markers 3 and 4, respectively. We see that the results calculated by the QGD algorithm



**Fig. 3.** Distribution of the longitudinal velocity component.

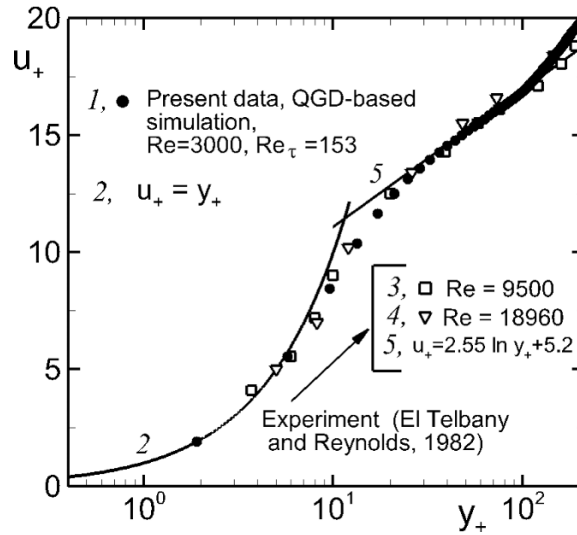


**Fig. 4.** Distribution of mean longitudinal velocity component in dimensionless variables.

and the experimental values hardly differ for different Reynolds numbers. Here and in what follows, the position of the markers 1 corresponds to the QGD grid.

According to the two-layer model of near-wall turbulence, the mean velocity profile is linear  $u_+ = y_+$  in the viscous sublayer  $y_+ < 5$  (curve 2) and logarithmic  $u_+ = A \ln y_+ + B$  for  $y_+ > 11$  (line 5). The following values have been obtained in [10] for the constants:  $A = 2.55$ ,  $B = 5.2$ . We see from Fig. 4 that in the range  $30 < y_+ < 100$  the QGD based simulation results virtually track the straight line  $u_+ = 2.55 \ln y_+ + 5.2$ . Thus, the QGD results provide an excellent description of the specific features of near-wall turbulence. The straight line also adequately fits the results of numerical simulation of Couette flow in [11].

Studies of turbulent Couette flow report different values for the constants  $A$  and  $B$ . Thus, the numerical simulations from [14] give a lower value  $A = 2.44$  compared with  $A = 2.55$  in [10], whereas  $B = 5.2$  as in [10]. The values  $A = 2.44$  and  $B = 5.0$  from [4, 15] and  $A = 2.44$  and  $B = 5.1$  from [16] are somewhat

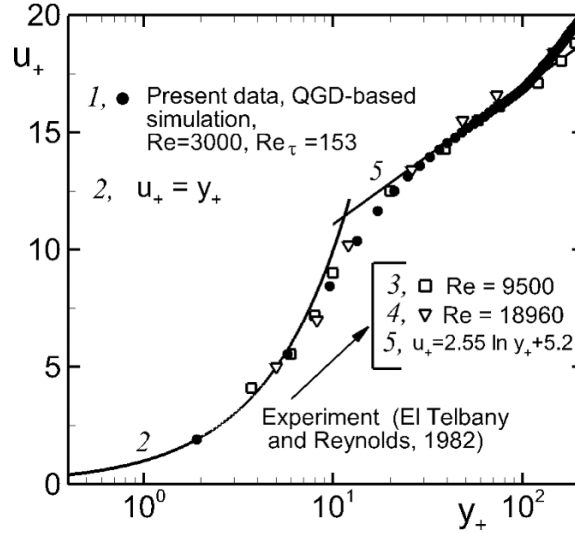


**Fig. 5.** Distribution of mean-square pulsations  $u'_x$  and  $u'_y$ .

lower than the values from [10]. Experimental studies find  $A = 2.55$  and  $B = 4.7$  in [12], compared with  $A = 2.50$  and  $B = 5.5$  in [13] for  $Re_\tau \approx 200$ .

We see from Fig. 4 that the results of QGD based calculations match the experimental data from [10] not only on the linear ( $y_+ < 7$ ) and logarithmic ( $y_+ > 12$ ) sections, but also in the transition zone  $7 < y_+ < 12$ .

Figure 5 shows the profiles of the mean-square velocity pulsations  $u'_x$  and  $u'_y$  versus the coordinate  $y$  normalized by  $L_y$ . Markers 1 denote the data of the present study. The pulsations  $u'_x$  have been calculated by the formula

$$u'_x = \left[ \frac{1}{n_{l2} - n_{l1} + 1} \left( \sum_{n_l=n_{l1}}^{n_{l2}} u_x^2 \right) - (u_x^m)^2 \right]^{1/2} \quad (37)$$

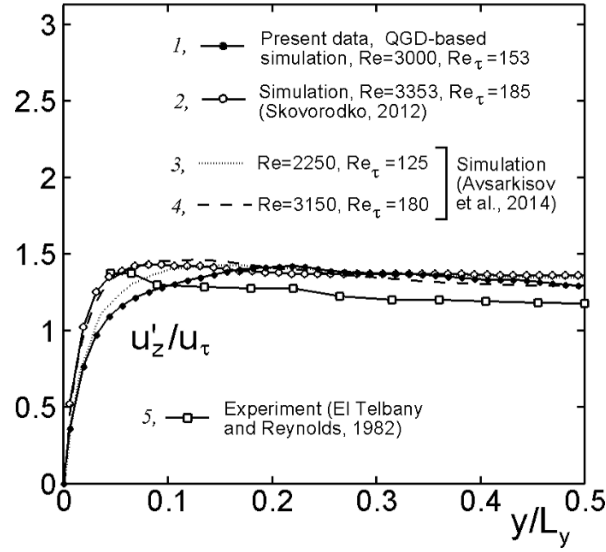
and are normalized by the dynamic velocity  $u_\tau$ . The pulsations  $u'_y$  and  $u'_z$  are determined similarly.

For comparison, Fig. 5 shows the mean-square pulsations obtained in [15, 16] for the simulation of Couette flow with close values of  $Re$  and  $Re_\tau$  (markers 2–4), as well as the experimental data from [10] (markers 5).

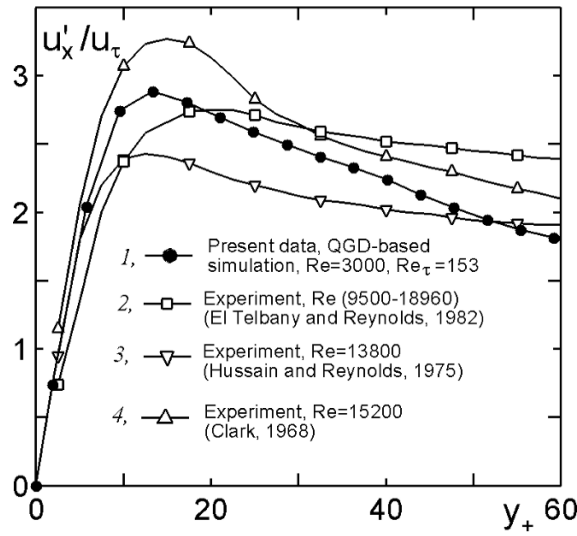
The maximum experimental values of  $u'_x$  obtained in [13] for Couette flow with Reynolds numbers from 2500 to 5000 fall in the range 2.8–2.9. These values are very close to the maximum value of  $u'_x$  obtained in the present study for  $Re = 3000$  (2.89) and to the numerical simulation results for  $Re = 3150$  from [16]. In [10], the experimental maximum value of  $u'_x$  is 2.75 (Fig. 7) and does not depend on the Reynolds number.

Figure 6 plots the mean-square pulsations  $u'_z$ . The notation is the same as in Fig. 5. The calculated and experimental results for  $u'_z$  show good fit.

Figure 7 shows the pulsations  $u'_x$  calculated in the present study (markers 1) and obtained experimentally (markers 2, 3, 4) as a function of the dimensionless coordinate  $y_+$ . Markers 2 combine the data from [10] for Reynolds numbers in the range 9,500–18,960. The data of [9] for  $Re = 13,800$  and the data of [8] for  $Re = 15,200$  are denoted by markers 3 and 4, respectively.



**Fig. 6.** Distribution of mean-square pulsations  $u'_z$ .



**Fig. 7.** Distribution of mean-square pulsations  $u'_x$  versus dimensionless coordinate.

While the experimental data are noticeably different, there is no clear dependence on the Reynolds number. Given the scatter of experimental data, the QGD simulation results show a reasonable fit with the experimental results.

In the present study we have used a very coarse uniform spatial grid. For  $Re = 3000$  the first four grid points (counting from the wall) have the coordinates  $y_+ = 1.91, 5.73, 9.54, 13.36$ . In [3], for DNS calculations of near-wall turbulence it is recommended to take a minimum spatial increment of  $\Delta y_+ = 1$  and to have not fewer than 3 points in the region  $0 < y_+ < 10$ . We see that the present study meets only the second condition. Despite the larger grid increment  $\Delta y_+ = 1.91$ , the QGD simulation results adequately match the experimental data for Couette flow.



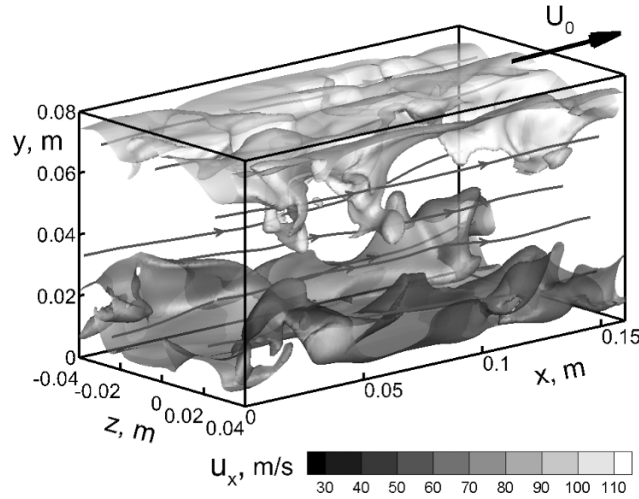


**Fig. 8.** Temperature isosurfaces and longitudinal velocity contours.

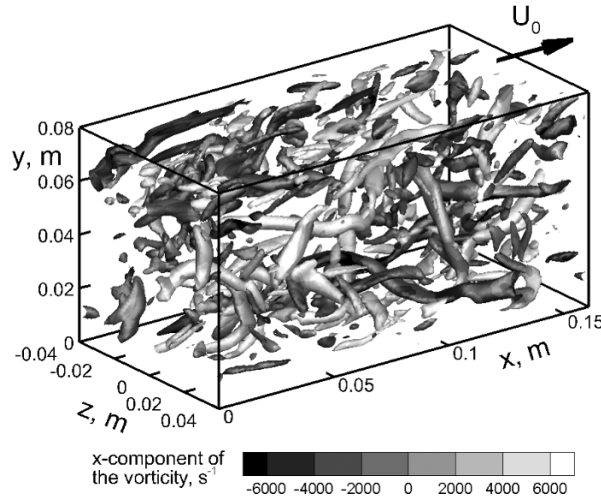


**Fig. 9.**  $Q$ -isosurfaces and contours of vorticity  $x$ -component.

To check the dependence of the numerical solution on the spatial grid increment, we have carried out a simulation for  $Re=3000$  on a coarser grid (spatial increment  $h=0.00125$  m, grid size  $N_x = 130$ ,  $N_y = 66$ ,  $N_z = 66$ ). The results are virtually identical to the data in Fig. 4, although  $\Delta y_+ = 2.26$ . In calculations with still coarser grids, no turbulent flow develops.

Note that most DNS studies of turbulent flows in channels use a much finer spatial grid. For instance, the viscous sublayer contains 11 grid point in [28] and 7 points in [22]. Thus, to obtain results comparable with DNS results, the spatial grid for the QGD algorithm should be chosen a factor of 3–5 coarser.

Figure 8 shows the temperature level surfaces for  $T = 299.7$  K in the numerical region. Note the increase of temperature from the initial value  $T_0 = 273$  K and also the wave-like temperature distribution. Contours of instantaneous longitudinal velocity  $u_x$  are superimposed on the temperature level surfaces. Furthermore, Fig. 8 shows the spatial streamlines. Since turbulent flow is characterized by vorticity, the spatial streamlines are not straight.

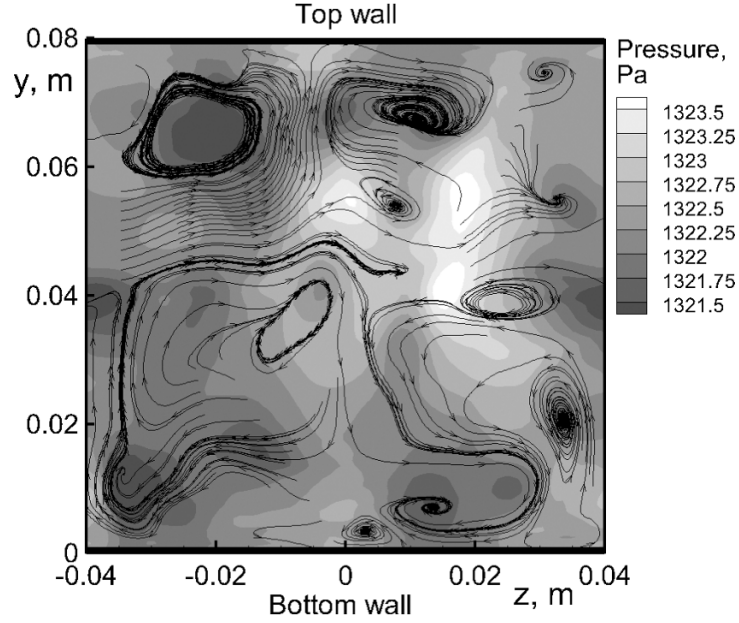


**Fig. 10.** Pressure contours and streamlines of transverse velocity components for  $x = 0.08$ .

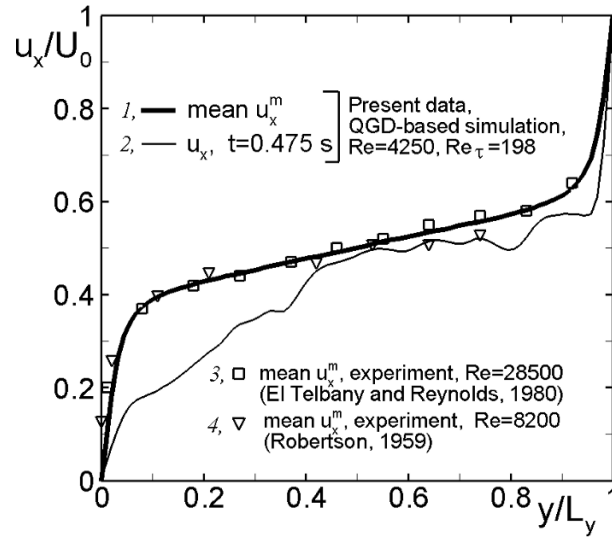


**Fig. 11.** Distribution of longitudinal velocity component.

Figure 9 shows the  $Q$ -level surfaces for  $Q = (\Omega_{ij}\Omega_{ij} - S_{ij}S_{ij})/2$ , where  $S_{ij} = (\partial u_i/\partial x_j + \partial u_j/\partial x_i)/2$  and  $\Omega_{ij} = (\partial u_i/\partial x_j - \partial u_j/\partial x_i)/2$  are the symmetrical and antisymmetrical parts of the velocity gradient tensor. These isosurfaces characterize coherent vortex structures in the flow field [2, 29, 30]. Contours of the vorticity  $x$ -component  $V_x = \partial u_z/\partial y - \partial u_y/\partial z$  are superimposed on the  $Q$ -level surfaces. We see numerous vortices, which is a normal feature of turbulent gas-dynamic flows.

Figure 10 shows the pressure contours in the cross-section  $x = 0.08$  and also streamlines of the transverse velocity components  $u_y$ ,  $u_z$  in the same cross-section. The vortex structure of the turbulent flow is clearly visible. There is noticeable spatial correlation between depressed pressure regions and the location of vortices.

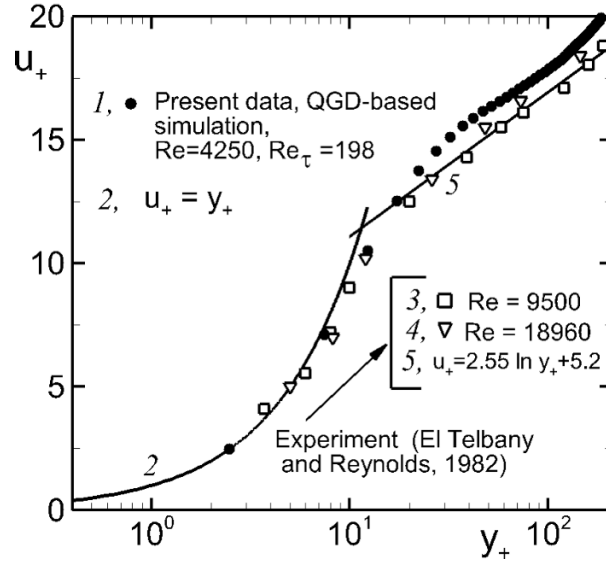


**Fig. 12.** Distribution of longitudinal velocity component in dimensionless variables.

## 6. Calculation Results for $Re = 4250$

Simulation by QGD based algorithm for  $Re = 4250$  has been carried out in the same way as for  $Re = 3000$ , with different initial values of density and pressure. Figure 11 is the longitudinal velocity profile. The notation and the experimental data are the same as in Fig. 3. The mean velocity profile for  $Re = 4250$  does not differ much from the profile for  $Re = 3000$  (Fig. 3) and also matches the experimental data.

A detailed analysis of the distribution of mean longitudinal velocity for  $Re = 4250$  (Fig. 12, notation as in Fig. 4) reveals somewhat higher velocities compared with the experimental data and also compared with the simulation results for  $Re = 3000$  (Fig. 4).

This deviation is possibly due to the excessively coarse numerical grid near the wall. For  $Re = 4250$  the first three grid point (counting from the wall) are  $y_+ = 2.47, 7.41, 12.36$ . Thus, the size of the spatial grid cells does not meet the criteria from [3]. Nevertheless, the simulation results using even such a coarse grid are in qualitative agreement with the experimental data. Flow simulation for large Reynolds numbers requires a finer spatial grid.

## 7. Calculation Results for $Re = 300$

For  $Re = 300$  the Couette flow is laminar (Fig. 5 from [10]). The QGD algorithm is uniformly applicable to both laminar and turbulent flows, as shown in [21]. There is no need to change any of the algorithm parameters; only the initial Reynolds number has to be changed.

In the present study we corroborate this property of the QGD algorithm in application to near-wall turbulence. Specifically, simulation with  $Re = 300$  leads to dissipation of the initial disturbance (1)–(2) and establishment of laminar Couette flow. The corresponding dependence of the kinetic energy on the current number of time steps is shown in Fig. 13.

We see from Fig. 13 that for  $Re = 300$  the gas kinetic energy in the numerical region becomes constant for  $n_t > 1.5 \cdot 10^5$ . The longitudinal velocity profile  $u_x$  becomes linear, as at the initial time (1). The initial disturb-

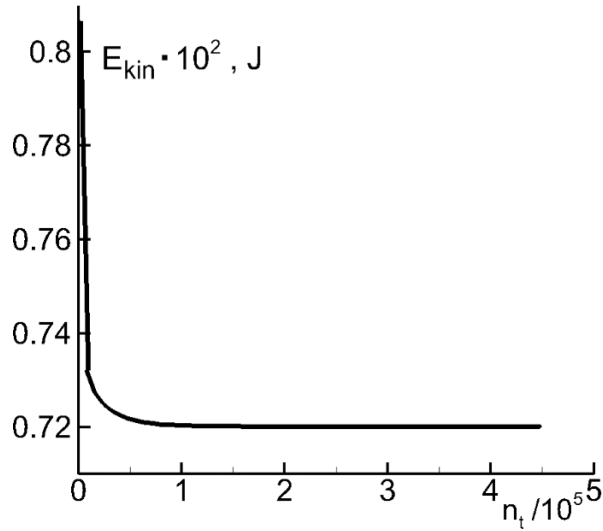


**Fig. 13.** Dependence of gas kinetic energy on the current number of time steps for  $Re = 300$ .

ance (2) almost completely disappears, so that the transverse velocity components do not exceed  $10^{-4}$  m/sec. Dissipation of the energy of the initial disturbance raises the gas temperature in the region up to 292 K.

Note that the same tuning parameter of the QGD algorithm  $\alpha = 0.1$  is applicable to both laminar and turbulent flows, far from the solid walls (Taylor–Green vortex) as well as in the near-wall region (Couette flow).

Satisfactory numerical simulation of laminar-turbulent transition in two-dimensional flow over a backward-facing step in a plane channel has been achieved for  $0.05 < \alpha \leq 0.3$  [31, 32].

## 8. Dependence of the Friction Coefficient on Reynolds Number

In laminar Couette flow the friction coefficient (defined in Table 3) is expressed by the formula

$$C_f = 2/Re^m. \quad (38)$$

Expression (38) can be obtained from the linear distribution of the longitudinal velocity component in laminar flow (1) and the definition of the averaged Reynolds number  $Re^m$  (Table 3).

In turbulent Couette flow, the friction coefficient can be approximated as [6, 10]

$$\sqrt{C_f/2} = G/\log_{10} Re^m. \quad (39)$$

In the present study, the dependences (38) and (39) are written in terms of the averaged Reynolds number  $Re^m$  instead of the initial  $Re$ . The expression for  $Re^m$  allows for the increase of dynamic viscosity as a result of temperature increase in the process of energy dissipation from the initial disturbance in compressible flow. The values of the Reynolds numbers and friction coefficient for three QGD-based simulations are presented in Table 4.

Different studies report somewhat different values of the constant  $G$  in (39). In [8],  $G = 0.19$ , and in [10],  $G = 0.182$ .

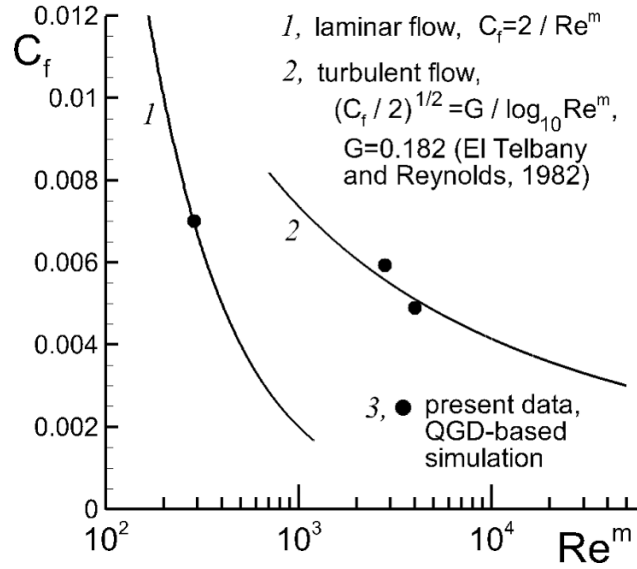


**Fig. 14.** Dependence of friction coefficient on Reynolds number.

Figure 14 plots the dependences (38) (curve 1) and (39) (curve 2) for  $G = 0.182$ , and also the data used in the present calculations from Table 4 (markers 3). The value  $G = 0.182$  from [10] satisfactorily fits the present results. Note that the experimental data for various investigations of Couette flow show pronounced scatter relative to the dependence (39) (Fig. 5 from [10]).

## 9. Conclusions

This study has demonstrated for the first time the possibilities of the QGD algorithm for the simulation of near-wall turbulent flows with moderate Reynolds numbers. For this purpose we have simulated turbulent ( $Re = 3000$  and  $4250$ ,  $Re_\tau = 153$  and  $198$ ) and laminar ( $Re = 300$ ) subsonic Couette flows in nitrogen.

We have shown that the QGD based algorithm adequately reproduces the near-wall velocity profile with fewer boundary layer points than in high-order DNS methods. Specifically, for  $Re_\tau = 153$  the uniform grid increment is  $\Delta y_+ = 1.91$  with 3 grid points in the viscous sublayer.

The practice of calculations and estimates [3] suggests that the spatial grid increment in the direction normal to the wall should be less than  $\Delta y_+ = 1$  near the wall and the number of grid points in the viscous sublayer should not be less than 7. Despite these restrictions, the longitudinal velocities produced by the QGD algorithms are virtually identical with the experimental values from [10] and the calculation results from [11].

The distribution of longitudinal velocity pulsations shows a better fit with experimental data than the DNS results from [15, 16]. Normal and transverse velocity pulsations match the results from [15, 16]. The  $Q$ -level surfaces reveal vorticity of the turbulent flow throughout the numerical region.

The QGD algorithm is suitable for simulating both turbulent and laminar near-wall flows. The laminar-turbulent transition is realized by changing the Reynolds number, which does not require any modification of the algorithm.

Given the present results, as well as the simulations of the Taylor–Green vortex from [21], we conclude that the QGD algorithm is highly promising for simulating both laminar and turbulent flows at moderate Reynolds numbers, far from the walls as well as in the near-wall region. Furthermore, the QGD algorithm describes flows

with shocks and can be efficiently parallelized. The QGD algorithm is thus useful for simulating the interaction of shocks with turbulent flows, including near-wall turbulence.

We acknowledge the valuable discussions with V. G. Priimak and P. A. Skovorodko on questions of simulation of near-wall turbulence.

Supported by the Russian Foundation for Basic Research Grant 16-01-00048.

## REFERENCES

1. H. Schlichting, *Boundary-Layer Theory*, McGraw-Hill, New York (1968).
2. M. Lesieur, *Turbulence in Fluids*, Springer (2008).
3. P. Sagaut, “Theoretical background: large-eddy simulation,” in: C. Wagner, T. Huttl, and P. Sagaut, editors, *Large-Eddy Simulation for Acoustics*, Cambridge University Press, Cambridge (2007), pp. 89–127.
4. S. Pirozzoli, M. Bernardini, and P. Orlandi, “Turbulence statistics in Couette flow at high Reynolds number,” *J. Fluid Mech.*, **758**, 327–343 (2014).
5. K. N. Volkov, “Formulation of wall boundary conditions in turbulent flow computations on unstructured meshes,” *Comput. Math. Math. Phys.*, **54**, No. 2, 353–367 (2014).
6. J. M. Robertson, “On turbulent plane Couette flow,” *Proc. 6th Midwestern Conf. Fluid Mech.*, Univ. Texas, Austin (1959), pp. 169–182.
7. M. M. M. El Telbany and A. J. Reynolds, “Velocity distributions in plane turbulent channel flows,” *J. Fluid Mech.*, **100** (part 1), 1–29 (1980).
8. J. A. Clark, “A study of incompressible turbulent boundary layers in channel flow,” *J. Basic Engineering*, **90**, 455 (1968).
9. A. K. M. F. Hussain and W. C. Reynolds, “Measurements in fully developed turbulent channel flow,” *J. Fluids Engineering*, **97**, 568–578 (1975).
10. M. M. M. El Telbany and A. J. Reynolds, “The structure of turbulent plane Couette flow,” *J. Fluids Engineering*, **104**, 367–372 (1982).
11. B. L. Rozhdestvenskii, I. N. Simakin, and M. I. Stoinov, “Modeling turbulent Couette flow in a plane channel,” *J. Appl. Mech. Tech. Phys.*, **30**, No. 2, 223–229 (1989).
12. K. Bech, N. Tillmark, P. Alfredsson, and H. Andersson, “An investigation of turbulent plane Couette flow at low Reynolds numbers,” *J. Fluid Mech.*, **286**, 291–325 (1995).
13. O. Kitoh, K. Nakabayashi, and F. Nishimura, “Experimental study on mean velocity and turbulence characteristics of plane Couette flow: low-Reynolds-number effects and large longitudinal vortical structure,” *J. Fluid Mech.*, **539**, 199–227 (2005).
14. T. Tsukahara, H. Kawamura, and K. Shingai, “DNS of turbulent Couette flow with emphasis on the large-scale structure in the core region,” *J. Turbulence*, **7**, No. 19 (2006).
15. P. A. Skovorodko, “Slip effects in compressible turbulent channel flow,” *28th International Symposium on Rarefied Gas Dynamics, 2012, AIP Conf. Proc. 1501* (2012), pp. 457–464.
16. V. Avsarkisov, S. Hoyas, M. Oberlack, and J. P. Garcia-Galache, “Turbulent plane Couette flow at moderately high Reynolds number,” *J. Fluid Mech.*, **751**, No. R1, (2014).
17. B. N. Chetverushkin, *Kinetic Schemes and Quasi-Gas Dynamic System of Equations*, CIMNE, Barcelona (2008).
18. Yu. V. Sheretov, *Continuum Dynamics under Spatiotemporal Averaging. SPC Regular and Chaotic Dynamics* [in Russian], Moscow-Izhevsk (2009).
19. T. G. Elizarova, *Quasi-Gas Dynamic Equations*, Springer, Dordrecht (2009).
20. M. V. Popov and T. G. Elizarova, “Smoothed MHD equations for numerical simulations of ideal quasi-neutral gas dynamic flows,” *Computer Physics Communications*, **196**, No. 348–361 (2015).
21. I. A. Shirokov and T. G. Elizarova, “Simulation of laminar–turbulent transition in compressible Taylor–Green flow basing on quasi-gas dynamic equations,” *J. Turbulence*, **15**, No. 10, 707–730 (2014).
22. V. G. Priimak, “Direct numerical simulation of spatially localized structures and wave motions in turbulent shear flows: Numerical requirements,” *Mat. Model.*, **20**, No. 12, 27–43 (2008).
23. G. A. Bird, *Molecular Gas Dynamics and the Direct Simulation of Gas Flows*, Clarendon Press, Oxford (1998).
24. H. W. Liepmann and A. Roshko, *Elements of Gasdynamics*, California Institute of Technology, John Wiley and Sons, New York, 1957.
25. T. G. Elizarova and I. A. Shirokov, “Numerical simulation of a nonstationary flow in the vicinity of a hypersonic vehicle,” *Math. Model. Comput. Simul.*, **4**, No. 4, 410–418 (2012).
26. T. G. Elizarova and I. A. Shirokov, “Direct simulation of laminar–turbulent transition in a viscous compressible gas layer,” *Comput. Math. Model.*, **25**, No. 1, 27–48 (2012).

27. *K-100 System*, Keldysh Institute of Applied Mathematics RAS, Moscow; Available at <http://www.kiam.ru/MVS/resourses/k100.htm>.
28. J. Kim, P. Moin, and R. Moser, "Turbulence statistics in fully developed channel flow at low Reynolds number," *J. Fluid Mech.*, **177**, 133–166 (1987).
29. J. Jeong and F. Hussain, "On the identification of a vortex," *J. Fluid Mech.*, **285**, 69–94 (1995).
30. J. Fang, Y. Yao, Z. Li, and L. Lu, "Investigation of low-dissipation monotonicity-preserving scheme for direct numerical simulation of compressible turbulent flows," *Computers & Fluids*, **104**, 55–72 (2014).
31. T. G. Elizarova and P. N. Nikolskii, "Numerical simulation of the laminar–turbulent transition in the flow over a backward-facing step," *Vestn. MGU, Ser. 3: Fiz. Astron.*, No. 4, 14–17 (2007).
32. T. G. Elizarova, P. N. Nikolskii, and J. C. Lengrand, "A new variant of subgrid dissipation for LES method and simulation of laminar-turbulent transition in subsonic gas flows," in: Shia-Hui Peng and Werner Haase, eds., *Advances in Hybrid RANS-LES Modeling*, Springer-Verlag, Berlin, (2008), pp. 289–298.